PROCEEDINGS OF THE SIXTEENTH SYMPOSIUM

ON

ELECTROMAGNETIC WINDOWS

June 9—11, 1982

Edited by

G. K. Huddleston

TECH

GEORGIA INSTITUTE OF TECHNOLOGY
A Unit of the University System of Georgia
ATLANTA, GEORGIA 30332

8364891

PROCEEDINGS OF THE SIXTEENTH SYMPOSIUM

ON

ELECTROMAGNETIC WINDOWS

June 9–11, 1982

Edited by

G. K. Huddleston

GEORGIA INSTITUTE OF TECHNOLOGY
A Unit of the University System of Georgia
ATLANTA, GEORGIA 30332

FOREWORD

The Sixteenth Electromagnetic Window Symposium marks 27 years of reg larly scheduled symposia on electromagnetic windows. The first seven sympos were held at Ohio State University. The Georgia Institute of Technology h hosted the symposium biennially since 1966, with the U. S. Air Force cohosting t symposia of 1966, 1968, and 1972.

The Steering Committee responsible for the team planning and coordinati of the symposium consisted of the following individuals from the Georgia Institu of Technology:

J. N. Harris, General Chairman
Engineering Experiment Station

J. D. Walton, Technical Program Chairman
Engineering Experiment Station

G. K. Huddleston, Publications Chairman
School of Electrical Engineering

H. L. Bassett, Publicity Chairman
School of Electrical Engineering

D. J. Kozakoff, Local Arrangements Chairman
Engineering Experiment Station

E. B. Joy, J. A. Fuller, and J. M. Newton

In addition, G. H. Adams and R. V. Eberwein of Continuing Education put significant efforts in the coordination of the meeting activities and mailing o brochures.

Papers not received in time for publication will be available durin meeting from either the registration desk or the particular author.

For the Steering Committee

A. K. Huddleston

G. K. Huddleston
Proceedings Editor

TABLE OF CONTENTS

AN EFFICIENT ELECTRICAL
ANALYSIS OF A BROAD-BAND
AXISYMMETRIC RADOME AND
BROAD-BEAM MULTI-MODE ANTENNA

David G. Burks
Antenna Laboratory
Texas Instruments Incorporated
P.O. Box 226015   M/S 333
Dallas, Texas   75266

This paper addresses the effects of an axisymmetric radome on the patterns of a spiral direction finding antenna. The multi-mode spiral antenna is characterized by circular-polarized far-field patterns of the form $p(\theta) \exp(jm\phi)$ where m is an integer mode number. Modes 1 and 2 are used for direction finding by the monopulse technique.

When the axes of the radome and antenna are the same, the symmetries of the fields and radome permit a very efficient analysis based on a conventional transmitting formulation. This method treats the tangential fields over the exterior surface as equivalent sources which are integrated to find the patterns. Computational efficiency is achieved by performing the azimuthal integration analytically. Thus, only an axial summation is required for the integration. The entire technique is modular, so changes may be made in the method for computing the wall transmission without effecting the surface integration. Also, consideration of interior wall reflection and tip scatter are easily incorporated. Results of the analysis using plane-wave, planar slab and spherical-wave, curved wall transmission coefficients are compared with measurements made on an asymmetrical A-sandwich radome.

1

ACCURACY OF METHODS FOR COMPUTING
RADOME ELECTROMAGNETIC EFFECTS

R. A. Hayward, E. L. Rope, G. Tricoles

General Dynamics Electronics Division, P.O. Box 81127, San Diego, CA 92138

INTRODUCTION

Comprehensive comparisons of measured and computed radome boresight error (BSE) appear lacking. This lack is understandable because BSE depends on many factors including the radome size, shape, and composition as well as the properties and orientation of the enclosed antenna, the frequency of the waves, their polarization, and direction of propagation.

In some earlier papers, we compared, measured, and computed BSE of three radomes that had distinct dimensions.[1,2] The frequency band was limited to a few percent. The radomes had length-to-diameter ratios of approximately two, but base diameters were approximately four, six and 10 wavelengths. The enclosed antennas had dimensions about a wavelength less than those of the radomes. The comparisons showed that a surface integration method, shown in Figure 1, gave accurate results, but that a direct ray method, also defined in Figure 1, failed for the smaller radomes. This conclusion was for a narrow bandwidth.

This paper describes additional tests of the surface integration method. The frequency band is wide; the radome shape is identical to one of those in Reference 1. Two accuracy criteria are utilized. One, boresight error, is conventional. The other is the complex-valued transmittance in the radome-bounded region; this quantity describes wavefronts. It is measured with a small probe antenna that scans the region behind the radome. The transmittance is significant because it is a direct measurement of the accuracy of descriptions of propagation through the radome. The transmittance is simpler than BSE, which results mathematically from an integral of the product of transmittance and the antenna's nearfield distribution.

BORESIGHT ERROR

Boresight error was computed with the integration method shown in Figure 1 and described in Reference 1. Results are in Figures 2 and 3.

The parameters were as follows. The radome had fineness ratio 2, with base diameter 5.5 wavelengths at the lowest frequency f_L. The radome thickness was $0.087\lambda_L$, where λ_L is the wavelength at f_L, and dielectric constant was 2.6. The enclosed antenna consisted of a pair of rectangular horns for the lower half of the frequency range; aperture dimensions were $1.5\lambda_L$ by $1.2\lambda_L$ and spacing was $1.5\lambda_L$. A second pair of horns

with dimensions λ_L by λ_L was utilized for the higher frequencies, but the horn separation was also $1.5\lambda_L$.

The horn antennas were connected to a hybrid junction to produce a monopulse difference pattern. Measurements were done by moving the transmitting antenna at the far end of the test range to track the monopulse null while the radome was pivoted. For the calculations, the angular shift of the null from its direction with the radome absent was taken to be boresight error.

Figures 2 and 3 show measured BSE for the E-plane and H-plane.

WAVEFRONTS

Complex valued transmittance was measured by moving a small probe antenna in the radome-bounded region with the horn antennas removed. The detector was a network analyzer.

Figure 4 shows measured phase. The figure also shows values computed by the surface integration and direct ray method.

GUIDED WAVES

The differences between measured and computed transmittance were calculated. Figure 5 shows an example. Also shown is a graph of intensity for a slab-guided wave, assumed to decrease as $\exp(-vd)$, where v is the attenuation coefficient and d is normal distance from the wall.

CONCLUSIONS

The surface integration method gave accurate results over a wide frequency band of 200% for a thin radome with fineness ratio 2, and minimum base diameter of 5.5 wavelengths. The complex valued transmittance was also computed with reasonable accuracy by surface integration; however, the direct ray method was inaccurate. Discrepancies between measured and computed transmittance are attributed to guided waves.

REFERENCES

1. R. A. Hayward, E. L. Rope, and G. Tricoles, "Accuracy of Two Methods for Radome Analysis", Digest 1979, AP-S Symposium, pp 598-601, IEEE Catalog No. 79 CH1456-3 AP.

2. G. Tricoles, R. A. Hayward, and E. L. Rope, "Measurement, Calculation, and Reduction of Radome Wave Aberrations", Digest 1981, AP-S Symposium, pp 603-607, IEEE Catalog No. 81 CH1672-5.

D. J. White and H. J. Banks
Michelson Laboratory
Naval Weapons Center, China Lake, California

INTRODUCTION
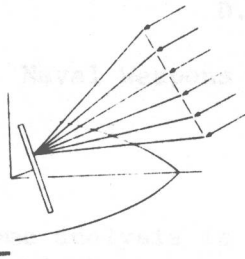
Figure 1. Surface Integration Method. Integration is Over Part of the Incident Wavefront. The Radome is Axially Symmetric. The Direct Ray Method Uses the Central Ray of the Bundle.

Figure 2. E-plane Boresight Error. Measured (–); Calculated (x).

Figure 3. H-plane Boresight Error. Measured (–); Calculated (x).

Figure 4. Phase Delay in Radome. Measured (–). Direct Ray Calculation (--).
Surface Integration with 49 Points Spaced by 0.6 Wavelength (x); by 0.8 Wavelength (0)

Figure 5. The Dots Show the Difference Between the Measured and Surface Integration Amplitudes. The Curve is Exponential Decay of a Guided Wave.

PLANE WAVE TRANSMISSION AND REFLECTION COEFFICIENTS FOR ANISOTROPIC SHEETS OF RADOME MATERIALS

D. J. White and D. J. Banks
Michelson Laboratory
Naval Weapons Center, China Lake, California 93555
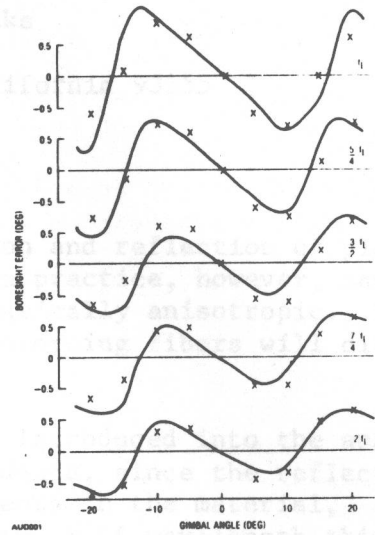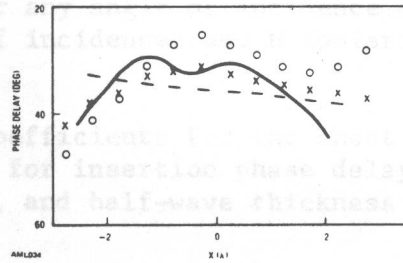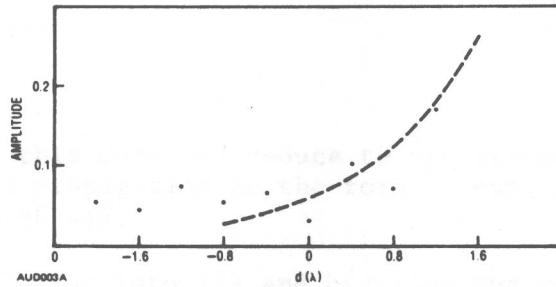
INTRODUCTION

Much radome analysis is based on the transmission and reflection of plane waves on isotropic homogeneous dielectric sheets. In practice, however, many materials, particularly composite dielectrics, are basically anisotropic. For example, the dielectric constant in the plane of reinforcing fibers will differ significantly from that normal to this plane.

If this anisotropy is neglected, errors will be introduced into the analysis, depending on the polarization and angle of incidence, since the reflection coefficients at the boundaries, propagation coefficients in the material, insertion phase delay, transmissivity and reflectivity, half-wavelength thickness, and Brewster's angle are all modified.

In this paper, an anisotropic dielectric sheet with dielectric constant ϵ_x in the plane of the sheet and ϵ_z normal to the sheet is considered. The sheet is uniaxial with the principal axis normal to the sheet. The normal modes for plane waves inside the material are found together with the reflection and transmission coefficients at the boundaries for any angle of incidence and for both E (polarized perpendicular to the plane of incidence) and H (polarized parallel to the plane of incidence) waves.

The overall reflection and transmission coefficients for the sheet are then derived, and simple expressions are given for insertion phase delay, transmissivity, reflectivity, Brewster's angle, and half-wave thickness [1].

THEORY

The problem to be solved is shown in Fig. 1, where a plane wave is incident at some angle of incidence, θ_i, upon an anisotropic sheet of thickness, d. Starting with Maxwell's equations and assuming harmonic time dependence with $\tilde{\epsilon}$ as the dielectric constant dyadic, given in this case by

$$\tilde{\epsilon} = \epsilon_x \hat{X}\hat{X} + \epsilon_x \hat{Y}\hat{Y} + \epsilon_z \hat{Z}\hat{Z} \quad , \tag{1}$$

a wave equation is derived:

$$\nabla \times \nabla \times \bar{E} = k_o^2 \tilde{\epsilon} \cdot \bar{E} \quad . \tag{2}$$

(Note that since $\nabla \cdot \bar{E} \neq 0$, this does not reduce to the standard $-\nabla^2 \bar{E}$ on the left-hand side.) We now assume propagation in the form $\bar{E}_o \exp(-j\bar{k} \cdot \bar{R})$, so that ∇ in Eq. (2) can be replaced with $-j\bar{k}$.

Substituting this solution into (2) and breaking the resulting vector equation into components results in three equations:

$$k_z^2 E_{ox} - k_x k_z E_{oz} = k_o^2 \varepsilon_x E_{ox} \tag{3a}$$

$$(k_x^2 + k_z^2) E_{oy} = k_o^2 \varepsilon_x E_{oy} \tag{3b}$$

$$k_x^2 E_{oz} - k_x k_z E_{ox} = k_o^2 \varepsilon_z E_{oz} \quad . \tag{3c}$$

On an actual radome, of course, the plane of incidence varies as a function of position on the antenna aperture; however, from Fig. 1, it is evident that the results will be independent of any rotation of the plane of incidence about the Z-axis. This is not true for anisotropic materials, in general, but holds for the uniaxial configuration treated here.

Equation (3b) is independent of E_{ox} and E_{oz}, and thus the solution for the E wave is

$$k_x^2 + k_z^2 = k^2 = k_o^2 \varepsilon_x \quad . \tag{4}$$

It follows immediately that all of the usual expressions for the transmission and reflection of waves polarized perpendicular to the plane of incidence are unchanged in form, with the provision that the dielectric constant in the plane of the sheet must be used.

In the case of Eqs. (3a) and (3c), for E_{ox} and E_{oz} to exist, the determinant of the coefficients must vanish. Since

$$k_x = k \sin\phi \quad \text{and} \quad k_z = k \cos\phi \quad , \tag{5}$$

this requirement results in

$$k^2 = (k_o^2 \varepsilon_x \varepsilon_z)/(\varepsilon_x \sin^2\phi + \varepsilon_z \cos^2\phi) \tag{6}$$

for the H wave. Manipulation of (3a) and (3b) then yields

$$E_{oz} = \varepsilon_{xz} E_{ox} \tan\phi \quad , \tag{7}$$

where $\varepsilon_{xz} = \varepsilon_x/\varepsilon_z$. Note that since $\bar{k} \cdot \bar{E} \neq 0$, the electric field is not orthogonal to the direction of propagation.

The next step is to find the reflection and transmission coefficients at the left-hand boundary. Referring to Fig. 1, this is equivalent to letting $d \rightarrow \infty$, and, for the H wave of interest, we may write

$$\bar{E}_i = E_{oix}(\hat{X} - \hat{Z} \tan\theta_i) \exp(-jk_o \hat{k}_i \cdot \bar{R}) \tag{8a}$$

$$\bar{E}_r = E_{orx}(\hat{X} + \hat{Z} \tan\theta_r) \exp(-jk_o \hat{k}_r \cdot \bar{R}) \tag{8b}$$

$$\bar{E} = E_{ox}(\hat{X} - \hat{Z} \varepsilon_{xz} \tan\phi) \exp(-jk \hat{k} \cdot \bar{R}) \tag{8c}$$

$$\bar{H}_i = (E_{oix}/\eta_o \cos\theta_i) \exp(-jk_o \hat{k}_i \cdot \bar{R}) \hat{Y} \tag{8d}$$

$$\bar{H}_r = (-E_{orx}/\eta_o \cos\theta_r) \exp(-jk_o \hat{k}_r \cdot \bar{R}) \hat{Y} \tag{8e}$$

$$H = \eta_o^{-1} \sqrt{\varepsilon_x/\varepsilon_z} \, (\varepsilon_x \sin^2\phi + \varepsilon_z \cos^2\phi)^{1/2} E_{ox} \exp(-jk \hat{k} \cdot \bar{R}) \hat{Y} \quad . \tag{8f}$$

The boundary condition requiring continuous tangential electric and magnetic fields is now applied. Thus,

$$E_{oix}\exp(-jk_o x \sin\theta_i) + E_{orx}\exp(-jk_o \sin\theta_r) = E_{ox}\exp(-jkx \sin\phi) \quad . \tag{9}$$

For Eq. (9) to be true for all x,

$$k_o\sin\theta_i = k_o\sin\theta_r = k\sin\phi \quad , \tag{10}$$

and Snell's law takes the form

$$\sin\theta = \sqrt{\epsilon_x\epsilon_z}\,\sin\phi/(\epsilon_x\sin^2\phi + \epsilon_z\cos^2\phi)^{1/2} \quad , \qquad \theta_i = \theta_r = \theta \tag{11a}$$

which can be manipulated to give

$$\cos^2\phi = \epsilon_x(\epsilon_z - \sin^2\phi)/((\epsilon_z - \epsilon_x)\sin^2\phi + \epsilon_x\epsilon_z) \quad . \tag{11b}$$

Our boundary condition equations now become

$$E_{oix} + E_{orx} = E_{ox} \tag{12a}$$

$$E_{oix} - E_{orx} = \sqrt{\epsilon_{xz}}\,(\cos\theta/\cos\phi)(\epsilon_x\sin^2\phi + \epsilon_z\cos^2\phi)^{1/2}E_{ox} \quad . \tag{12b}$$

It follows that

$$E_{ox}/E_{oix} = t_H = 1 + r_H \quad , \tag{13a}$$

with [2]

$$r_H = (\sqrt{\epsilon_z - \sin^2\theta} - \sqrt{\epsilon_x\epsilon_z}\,\cos\theta)/(\sqrt{\epsilon_z - \sin^2\theta} + \sqrt{\epsilon_x\epsilon_z}\,\cos\theta) \quad . \tag{13b}$$

At the right-hand (z = d) boundary in Fig. 1, we can again match boundary conditions or simply invoke what we know about the symmetry of the reflection coefficient — $r = (Z_L - Z_o)/(Z_L + Z_o)$ — Z_L being the load impedance and Z_o the characteristic impedance. Either way, the reflection coefficient at the dielectric-to-air boundary is $-r_H$, and the transmission across that boundary is $1 - r_H$.

The overall transmission and reflection coefficients for the dielectric slabs can now be written in standard form:

$$T = (1 - r_H^2)\exp(-jk_z d)/[(1 - r_H^2\exp(-2jk_z d)] \tag{14a}$$

$$R = r_H[1 - \exp(-j2k_z d)]/[1 - r_H^2\exp(-2jk_z d)] \quad . \tag{14b}$$

From (5), (6), and (11c) we see that

$$k_z = k_o\sqrt{\epsilon_{xz}(\epsilon_z - \sin^2\theta)} \quad , \tag{15}$$

which reduces to the standard form when $\epsilon_{xz} = 1$.

The half-wave window expression is given by $2k_z d = 2N\pi$, N an integer, or

$$d = N\lambda_o/2\sqrt{\epsilon_{xz}(\epsilon_z - \sin^2\theta)} \quad . \tag{16}$$

Brewster's angle is found by setting $r_H = 0$, or

$$\tan\theta_B = \sqrt{\varepsilon_z(\varepsilon_x - 1)/(\varepsilon_z - 1)} \quad . \tag{17}$$

Rearranging Eqs. (14), the insertion phase delay is

$$\text{I.P.D.} = k_o d \cos\theta - \tan^{-1}\{[(1 + r_H^2)/(1 - r_H^2)]\tan k_z d\} \quad , \tag{18a}$$

the transmissivity,

$$|T|^2 = (1 - r_H^2)^2/[(1 - r_H^2)^2 + 4r_H^2 \sin^2 k_z d] \quad , \tag{18b}$$

with reflectivity,

$$|R|^2 = 4r_H^2\sin^2 k_z d/[(1 - r_H^2)^2 + 4r_H^2\sin^2 k_z d] \quad , \tag{18c}$$

and phase shift on reflection of

$$\phi_R = \tan^{-1}\{[(1 - r_H^2)/(1 + r_H^2)]\cot k_z d\} - \pi \quad . \tag{18d}$$

Note that the far-right-hand term of (18a) is the phase shift, θ_T, on transmission.

We now have simple expressions, differing only slightly from the usual ones, allowing easy calculation of the quantities of interest for a uniaxial sheet, given the anisotropic dielectric constants, thickness, frequency, and angle of incidence for either polarization.

RESULTS

Using a partially dielectric-filled rectangular X-band waveguide cavity, ε_x and ε_z have been measured for some materials by cutting samples such that the E-fields would lie in the X- or the Z-direction. The results are shown in Table 1.

TABLE 1.

Material	ε_x	ε_z
3M, 300 board	2.85	2.41
Rogers RT, Duroid grade D-5880 (175K5)	2.19	2.29
NADC experimental laminate	3.07	2.66

REFERENCES

[1] Techniques for Airborne Radome Design, Vol. 1. T. E. Tice, Ed. Chapter 2, Section F, pp. 55–60, AFAL-TR-66-391, AD 811355, Dec. 1966. (At the time of the original submission of this paper, January 1982, the authors were not aware of the treatment (in Ref. 1) of this problem. It appears to us that the treatment given here should be considerably easier to apply and understand. Only small modifications to the usual expressions for transmission and reflections are required, and once these are made, the same expressions and programs can be used for both isotropic and uniaxially anisotropic sheets.)

[2] Ibid, Chapter 2, Section A, pp. 29–30. (The relationship between this reflection coefficient and the one for isotropic materials (in Ref. 2) is evident. The sign is opposite to that often used; this is because we have defined reflection in terms of E_x instead of H.)
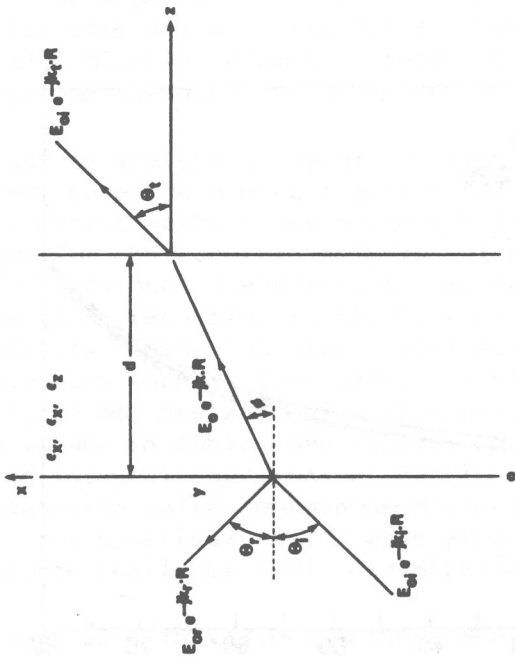
FIGURE 2. Normalized Thickness to Wavelength Ratio, 0.15.

NADC LAMINATE
Er=3.07, Er=2.06
Ex=Er=3.07
Ex=Er=2.06
D/WL=0.15

FIGURE 1. Transmission and Reflection of Plane Wave at Arbitrary Angle of Incidence on Uniaxially Anisotropic Slab.

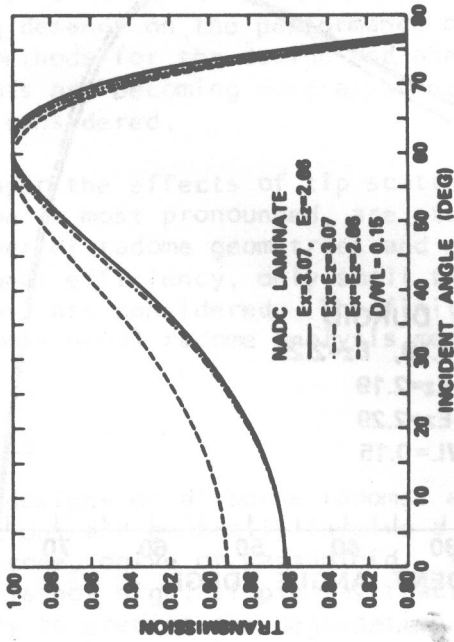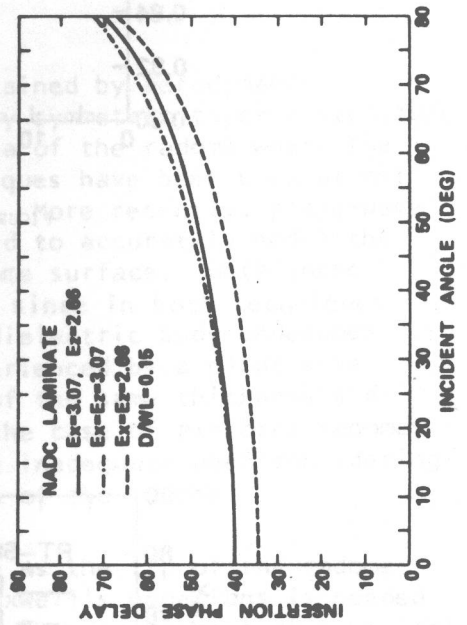FIGURE 3. Insertion Phase Delay Versus Incident Angle.

NADC LAMINATE
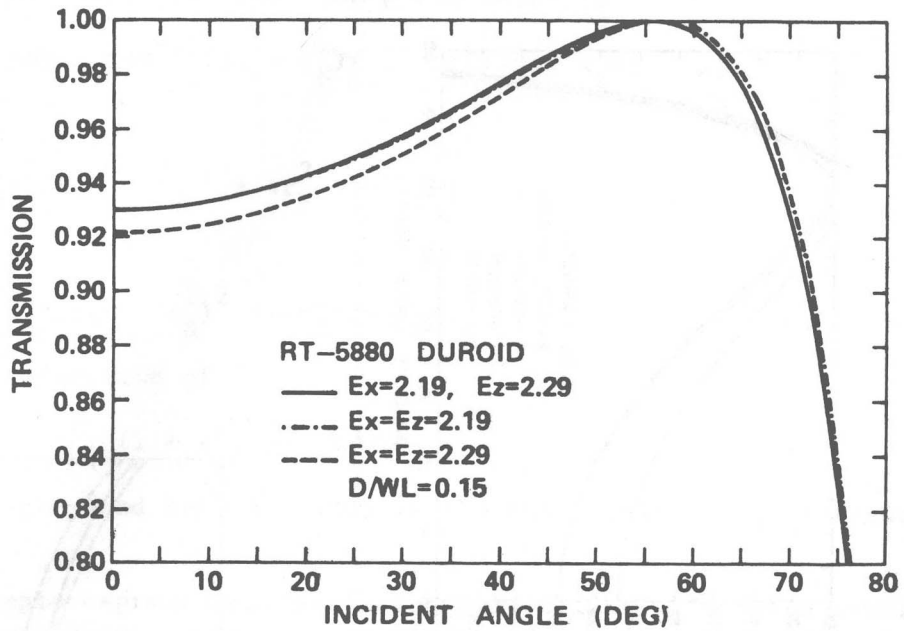Er=3.07, Er=2.06
Ex=Er=3.07
Ex=Er=2.06
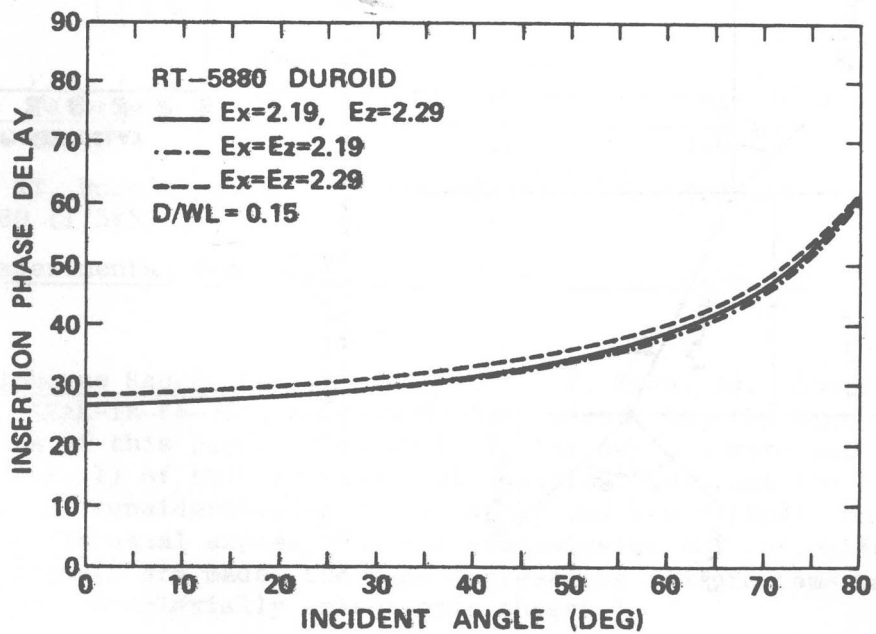D/WL=0.15

11

FIGURE 4. Transmission Versus Incident Angle.

FIGURE 5. Insertion Phase Delay Versus Incident Angle.

12